

Aerial observations of sea ice break-up by ship waves

Dumas-Lefebvre Elie¹ and Dumont Dany¹

¹Institut des sciences de la mer de Rimouski, Université du Québec à Rimouski, 310 allée des ursulines, Rimouski, QC, Canada G5L 3A1

Correspondence: Elie Dumas-Lefebvre (elie_dumas-lefebvre@uqar.ca)

Abstract. We provide high resolution in situ observations of wave-induced sea ice breakup in the natural environment. In order to obtain such data, a drone was deployed from the Canadian Coast Guard Ship *Amundsen* as it sailed in the vicinity of large ice floes in Baffin Bay and in the St. Lawrence Estuary, Canada. The footage obtained from these experiment was used to obtain the floe size distribution (FSD) and the temporal evolution of the break-up. FSDs are then compared to theoretical fracture lengthscale, one being based on flexural rigidity of sea ice and the other, on the incident wavelength. Floe-area-weighted FSDs exhibit a modal shape, thus indicating that a preferential size is generated by wave-induced breakup. Furthermore, the increase of the mode with greater thickness show that ice thickness plays a defined role in determining the preferential size. Comparison with relevant theory suggests that the maximum floe size is dictated by not only by the ice rigidity but also by the incident wavelength. It was also observed that the in-ice wavelength is smaller than the estimated incident wavelength, thus suggesting that waves responsible for the break-up obey to the mass loading dispersion and that the break-up advances almost as fast as the wave energy. Moreover, the observed break-up extents show that thicker ice can attenuate wave less than thinner ice. Overall, this dataset provides key information on wave-induced sea ice break-up and highlights the potential for better understanding the physics of natural sea ice in response to waves.

1 Introduction

The marginal ice zone (MIZ) is the ice-covered region that is affected by waves, usually found in the periphery of the polar and subpolar oceans. Reductions of Arctic sea ice thickness and summer extent in response to global warming (Kwok and Rothrock, 2009; Cavalieri and Parkinson, 2012) generally contribute to increase the extent of the MIZ (Horvat and Tziperman, 2015; Squire, 2020). The decrease of the summer minimum extent at a rate of 10% per decade over the last 30 years (Comiso et al., 2008) provides larger fetch to increasingly frequent cyclones (Rinke et al., 2017), which generate a more energetic wave field in the Arctic basin (Smith and Thomson, 2016; Stopa et al., 2016; Li et al., 2019; Thomson and Rogers, 2014; Casas-Prat and Wang, 2020). The increasingly energetic waves may then have greater potential to break-up sea ice thus generating a larger MIZ. That way, changes in sea ice dynamics and in ocean-atmosphere heat exchanges could be observed at the large scale.

By fracturing large pieces of sea ice into smaller ones, waves change the floe size distribution (FSD) locally and thus contribute to an increase in the total lateral sea ice surface being in contact with water. This results in a greater total sea ice perimeter and in the exposure to the atmosphere of water areas that were previously capped under a layer of sea ice. During the melt season, both the increase of the total ice perimeter and the lower albedo caused by the exposure of darker waters

can increase the melt rate (Steele, 1992). On the other hand, enhanced heat loss from the ocean to the atmosphere due to the creation of leads and cracks can promote ice formation in cold conditions.

30 A fragmented ice cover can also have a significantly different dynamical response to external forces, as discussed by Dumont et al. (2011). Herman et al. (2021) report with great detail, using high resolution satellite imagery, how waves broke up a very large ice floe into much smaller ones, and how easily they drifted and deformed in response to wind, waves and current. Floe size is also important for constraining some parameterizations of wave propagation and attenuation, although it is still unclear whether and how it is significant in reality. For instance, it determines the flexural response of the ice cover, and consequently the possible scattering of wave energy (Squire, 2007). Wave scattering by sea ice can be important especially when floe size is comparable or larger than the wavelength (Kohout and Meylan, 2008; Bennetts et al., 2010; Squire, 2018). It also determines the importance of energy dissipation through inelastic and anelastic strain (Boutin et al., 2018).

The FSD is an undoubtedly important parameter for sea ice dynamics, such that there has been great efforts to quantify it. Yet, to our knowledge, there are no observational studies that directly relate the FSD to the processes that generated it in the natural environment. Most observations come from satellite or aerial imagery of Arctic and Antarctic MIZs where observable floes have an unknown history (Weeks et al., 1980; Rothrock and Thorndike, 1984; Holt and Martin, 2001; Toyota and Enomoto, 2002; Toyota et al., 2006, 2011; Lu et al., 2008; Herman, 2010; Alberello et al., 2019; Herman et al., 2021). After identifying the boundaries of individual ice floes, either manually or using autonomous image processing algorithms, a characteristic length scale is determined and used as a metric for the *floe size*. The FSD is represented either as a number density (ND) or as a probability density function (PDF). The former approach, which is the most widely used, takes the form of a continuous curve relating the number of floes per square kilometers to the floe size in a cumulative or non-cumulative way (see Figure 1 of Stern et al., 2018). In the second approach, floe size categories are given a probability of occurrence based on the frequency of observation in order to represent the FSD as an histogram. It appears from the above-mentioned studies that when represented as a ND, the FSD generally follows a power law of the form $n(d) \propto d^{-\gamma}$ where n is the number of floes having a characteristic floe size d . This type of distribution has been tied to the fractal and possibly scale invariant morphology of fractured sea ice Rothrock and Thorndike (1984), and sometimes presented as a path for understanding the broad characteristics of underlying physical processes (Herman, 2010). A review of the available FSD observations and of the power law is made by Stern et al. (2018). In the end, these observations give a large scale view of the MIZ morphology and can give information on the seasonal evolution of the FSD. However, both the low temporal resolution of satellite images and the sparseness of aerial observations do not allow, for example, to capture the contribution of individual break-up events to the overall FSD.

55 Large-scale spectral Wave-Ice models (WIMs) (Dumont et al., 2011; Williams et al., 2013a, b; Zhang et al., 2016; Bennetts et al., 2017; Boutin et al., 2018; Bateson et al., 2020; Boutin et al., 2020) use a power-law FSD to estimate sea ice morphological properties such as the mean floe size. Such statistical moments are dependent on the shape of the FSD and are further used to parameterize numerous MIZ processes, such as the lateral melt. This allows studying floe-size dependent processes on sea ice dynamics, which represents a necessary step for improving global climate models and climate projections. However, by simplifying and idealizing how MIZ processes affect the shape of the FSD, these models do not represent a physically-based solution of the MIZ dynamics but rather the effects of including a FSD obeying prescribed rules on the evolution of a sea

ice cover (Herman, 2017). For example, Dumont et al. (2011), Williams et al. (2013a), Williams et al. (2013b), Boutin et al. (2018), Bateson et al. (2020) and Boutin et al. (2020) all model the influence of break-up by updating the maximum floe size (d_{\max}) of a power-law FSD even though there is no empirical evidence showing that this is how fragmentation affects the shape of the FSD.

Focusing on the process of break-up itself rather than on its influence on dynamics, Fox and Squire (1991) studied the propagation of strain into an ice sheet. Modeling sea ice as a thin, semi-infinite elastic plate, they obtained that "*the position [of maximum strain] depends crucially on ice thickness and to a lesser extent on wave period*". On the other hand, Herman (2017), by modeling the ice cover as a strip of discrete cubic-shaped grains being linked by elastic bonds, obtained that "*breaking of a continuous ice sheet by waves produces floes of almost equal size, dependent on thickness and strength of the ice but not on the characteristics of the incoming waves*". By coupling a two-dimensional flexural breakup model to a three-dimensional model of wave scattering by circular floes, (Montiel and Squire, 2017) found out that either a modal or bimodal FSD was generated from wave-induced sea ice breakup, thus also suggesting that a preferential size is generated from breakup. More recently, Mokus and Montiel (2021) created a 2-D hydrodynamic model for wave-induced sea ice breakup which combines linear wave theory and viscoelastic sea ice rheology in order to compute the scattering of wave by sea ice floes. Using an empirical strain threshold to define the floe size resulting from breakup, they obtained that the FSD follows a lognormal distribution under realistic wave forcings thus demonstrating that a preferential size is indeed generated by the process. They also show that the median floe size evolves with both wave period and ice thickness, result that partly contrasts with the findings of Fox and Squire (1991) and Herman (2017) in which the FSD is independent of the sea state.

In the end, there seems to be a consensus from process-based model studies towards the fact that a preferential size is generated by wave-induced sea ice breakup and that the observed power law does not come out from this process alone. However, it is still unclear what the respective contributions of sea ice rigidity and wave properties are in determining the preferential size and the shape of the FSD. The question remains as to whether these theoretical conclusions are supported by field observations.

Although there has been significant efforts to model the break-up process, only few studies have approached the problem from an observational perspective (e.g. Langhorne et al., 1998; Kohout et al., 2014, 2016a). Furthermore, little attention has been put towards the analysis of the resulting FSD and its possible connection to sea ice flexural rigidity and to waves properties (Toyota et al., 2011). The first anecdotal observations of wave-induced breakup were reported in Squire (1995) where he states that "*the width of the strips [...] created by the process is remarkably consistent and appears [...] to be rather insensitive to the spectral structure of the sea but highly dependent on ice thickness*". In other words, he observed that the distance between successive cracks generated by break-up seems to be constant and independent from the sea state but rather dependent on the material properties of sea ice. This remark qualitatively supports the conclusions of Fox and Squire (1991) and Herman (2017), but quantitative analysis of observational data is required to fully test these hypotheses. More recently, Herman et al. (2018) carried out break-up experiments in large tanks where waves were generated artificially to break apart a layer of laboratory-grown ice with the goal of testing the conclusions of Herman (2017) and Squire (1995) on the independence of the break-up pattern on wave properties. Herman et al. (2018) compared the mean sizes obtained from the experiments to a theoretical

fracture distance x^* derived by Mellor (1983), which is solely dependent on the flexural rigidity of the ice. For a group of experiment (group A test 2060), the value of x^* was close to the mean size which lead Herman et al. (2018) to conclude that "*the floe size resulting from breaking by waves depends not on the incoming wavelength, but rather on the mechanical properties of the ice itself*". Unfortunately, a factor of $\frac{1}{2}$ was omitted in the mathematical expression of x^* (as is demonstrated in section. 5.1) so that this conclusion needs to be revisited. Hence, observations of wave-induced sea ice break up in the natural environment are needed since available laboratory and field studies do not paint a complete picture of the respective role of sea ice and wave properties on determining the shape and extent of the FSD arising from this process.

Few field studies about natural break-up have been made yet mainly because the MIZ is an arduous area to sample directly from. It is indeed hard to be in the MIZ at the right place and at the right time, with good but not too harsh weather conditions for break-up to happen, and with the right apparatus and available people to measure all relevant variables during a natural break-up event. Indeed it is possible to study wave-ice interactions in the laboratory but it is not clear if the results directly apply to the natural environment owing mostly to the complex life history of naturally-grown sea ice compared to the more homogeneous growth conditions of the laboratory.

Rather than waiting for the stars to be aligned in the natural environment, we chose to create waves with a ship in order to simulate breakup events. With the help of a unmanned aerial vehicle (UAV or drone) and image processing, the breakup experiments conducted in the Gulf of Saint-Lawrence (GSL) and in the northern Baffin Bay (NBB) allowed us to measure the outcome of small period waves breaking naturally grown sea ice. While no apparatus measuring curvature of the ice or incident wave properties were successfully deployed, it was possible to extract information about the resulting FSD, the breakup speed and its extent. When compared to thin elastic plate theory, these results give insight on the underlying physics of wave-induced sea ice breakup.

2 Methods

The setup for the experiments conducted to obtain FSDs resulting from wave-induced breakup is as follows. First, a large level ice floe having a side exposed to open water is identified. Then a UAV is deployed and positioned above the ice edge to record high resolution footage of the break-up event. Finally, the Canadian Coast Guard Ship (CCGS) *Amundsen* cruises near the floe edge at a high and constant speed such that waves are generated in the vicinity of the ice. Two experiments are carried out, the first one in February 2019 in the GSL and the second in August 2019 in NBB. In both experiments, no wind-generated wave nor swell were present, hence the observed break-up can only be attributed to ship-generated waves. The use of a ship for these experiments provides a better management of weather conditions for drone deployments while still allowing to study break-up in the natural environment. Such a setup also allows to have no constraint on the location of deployments and to search for the right sea ice to break. A DJI Mavic 2 Pro is used for both experiments because of its autonomy, resilience to cold temperature, hovering stability and high resolution camera. The camera has a 65.5° field of view and a sensor that record photos at a resolution of 20 Mpx and 4K videos. The camera is factory-calibrated by DJI. While its height relative to the takeoff location is obtained by a barometric sensor, it uses both GPS and GLONASS for geopositioning, hovering in a still position

130 and correcting its altitude. The error on its vertical and horizontal position are respectively of 0.5 and 1.5 m. The specifics of each experiment are described below.

2.1 Gulf of St. Lawrence

The first experiment was conducted in the northwestern Gulf of St. Lawrence (GSL), Canada, at (49.584°N, 66.152°W) on 7 February 2019 which was a clear, calm and cold day ($T_{\text{air}} = -7.2^{\circ}\text{C}$). According to the ice chart produced by the Canadian Ice Service (CIS) on the same date, there was a 9/10 sea ice concentration that consisted in grey (4/10) and grey-white ice (5/10).
135 These stages of development are associated to thicknesses between 10 and 30 cm. The thickness of the floe we selected for the experiment was estimated visually looking at the ice free board from the lower deck of the ship ~ 3 m above the surface, since it was not possible to measure the ice thickness directly. Given the available information and the level of uncertainty, we estimate the thickness of the ice floe as 20 ± 10 cm.

140 Figure 1 shows the schematic of the GSL experiment. The *CCGS Amundsen* accelerated and reached an average speed of 7.25 m s^{-1} less than 50 m from the region of interest, thereby generating a wave train with an amplitude that was sufficient to break up the ice floe. The ship speed over the portion of the trajectory that generated the observed waves remained relatively uniform, with a standard deviation of 0.08 m s^{-1} . Oblique sunlight conditions allowed us quantifying the wavelength, the period and the direction of the waves (see section 3.2). Unfortunately, we could not deploy any wave sensor on the ice or in the
145 water so that we can't quantify wave amplitude during the experiment. A metric conversion factor of $3.1 \pm 0.04 \text{ cm px}^{-1}$ was assessed from the UAV's altitude and field of view (FOV) by considering the manufacturers uncertainty of ± 0.5 m on altitude and by taking into account an error of $\pm 0.5^{\circ}$ for the FOV.

2.2 Northern Baffin Bay

The second experiment was conducted in northern Baffin Bay (NBB) at (77.883°N, 77.341°W) on 5 August 2019 in cloudy
150 conditions and above freezing air temperature $T_{\text{air}} = 4.9^{\circ}\text{C}$. According to the ice chart produced by the Canadian Ice Service (CIS) on this day, ice concentration was 4/10 and the ice thickness was identified to be between 30 and over 120 cm as thin and thick first year ice were indicated to be present. The floe chosen for the experiment consisted in a plate of heavily rotten first year ice of about 540-m wide and more than 2-km long. With the help of a zodiac boat onboard the *CCGS Amundsen*, the ice thickness was measured on floes resulting from the breakup using a meter stick with a hook at one end. The thickness was
155 assessed to be between 40 and 60 cm.

Figure 2 describes the experimental setup in NBB. The average speed of *CCGS Amundsen* evaluated during its passage near the floe is 8.37 m s^{-1} with a standard deviation of 0.05 m s^{-1} . In this experiment, an attempt was made to deploy wave buoys on the ice with the zodiac before waves hit and fractured the floe. Two SKIb wave buoys (Guimarães et al., 2018) were installed on the floe 2 to 3 m of the edge and roughly 10 m apart in order to measure the wavelength. The zodiac then went at a safe
160 distance from the ice floe to launch the UAV. Unfortunately, overwash from the primary wave pushed and flipped the buoys such that their data is unusable. The propagation of flexural waves in the ice floe could not be observed visually due to the flat lighting conditions of an overcast sky. No in-ice wave properties could be measured. The UAV took pictures of the fragmented

ice floe after the passage of the waves. These pictures were used to generate an orthomosaic picture of a portion of the broken floe using the open source software Open Drone Map (ODM), with a resolution of 5 cm px^{-1} .

165 3 Image processing

3.1 Sea ice segmentation

The detection of sea ice floes in each orthomosaic consists of a series of steps that are illustrated in Figure 3. First the RGB image is converted to grayscale, with values from 0 to 255. From the histogram of the grayscale image, an intensity threshold separating dark water pixels from bright ice pixels is used to create a binary images where 1 indicates ice and 0 indicates water. For many reasons, this binary map does not perfectly separate ice and water, and each ice floe from their neighbors. The presence of slush or very small ice fragments in between floes can merge many floes into a larger one. Conversely, wet ice can generate holes in floes. To circumvent these imperfections, various segmentation algorithms have been developed and applied in similar contexts, namely the morphology gradient (Zhang et al., 2012), the watershed transform (Meyer, 1994; Zhang et al., 2013) or the gradient vector flow (Zhang and Skjetne, 2014, 2015). We refer the reader to Zhang and Skjetne (2018) for a good review of image processing methods that are applicable to sea ice segmentation.

Here, the method that gives the best results is the watershed transform (Meyer, 1994). It uses the Euclidean distance transform of the first binary map to generate a topographic map for each individual object. When two objects are in contact, the two watersheds connect through a *valley*. If this valley is deeper than some chosen threshold depth, then the two watersheds are segmented across that valley and the original floe is separated in two. This method can sometimes generate new floes, under-segment or over-segment existing floes (Zhang and Skjetne, 2018), but it is possible to circumvent these issues with fine adjustments. To avoid over-segmentation, local minima in the distance transform are removed. To avoid under-segmentation, successive morphological erosion and dilation steps are applied to separate floes that are in contact. Finally, only objects with an isoperimetric ratio $\Gamma = P^2/4\pi A$ smaller or equal to 3.5 are identified as floes for further analysis.

Similarly to Herman et al. (2018), floes having a horizontal dimension that is close to their thickness are removed, since they can't be generated by flexural failure. In the GSL experiment, $h = 20 \pm 10 \text{ cm}$. Thus, floes having a surface area $A \leq 900 \text{ cm}^2$ are removed. For the NBB experiment, $h = 50 \pm 10 \text{ cm}$ and floes with $A \leq 3600 \text{ cm}^2$ are removed. A thorough visual examination of the final binary image of the GSL experiment shows that it corresponds well to the initial image so that morphological properties of sea ice floes can be extracted from it. For the NBB experiment, the omnipresence of large melt ponds at the surface of the floes made it impossible to detect efficiently sea ice boundaries using the watershed transform method. Images were thus manually segmented. Using the Matlab Image Processing Toolbox, numerous morphological properties of sea ice floes are extracted. For instance, each floe is fitted to an ellipse of major axis length a , minor axis length d (Fig. 4), which is indicative of the distance between cracks induced by the highest amplitude wave. Following Squire (1995) and Herman et al. (2018), the minor axis length is thus chosen as the floe size since it represents the characteristic break-up length scale.

3.2 Break-up evolution

195 Using drone footage in the GSL, it was possible to estimate the wavelength and the wave period due to favorable lighting conditions provided by the oblique sunlight. The in-ice wavelength λ is obtained from a visual estimation of the distance between two consecutive wave crests. The period T is obtained from a Fourier transform of the time series of the mean brightness in a region of interest. (dashed rectangle in Figure 5). The wave phase speed is then obtained by $c_p = \lambda/T$.

The speed of the break-up front is evaluated using an automated and unsupervised algorithm that identifies the furthest
200 fracture point along each of the colored lines in the direction of wave propagation shown in Figure 5. The algorithm computes the brightness as the mean of the image RGB values and finds the furthest pixel having a brightness value under 90, the maximum being 255. This threshold is chosen manually after verification with a limited number of frames, and the algorithm is applied every 0.2 s. The break-up speed is then obtained as the slope of the linear regression relating fracture distance to elapsed time.

205 4 Results

4.1 Waves and break-up

Table 1 presents a summary of the physical parameters that were measured and estimated in both experiments. In the GSL experiment, the wave period measured from brightness variations in the UAV footage is $T = 4.0 \pm 0.2$ s (Fig. 5). The in-ice wavelength is $\lambda_{\text{ice}} = 19.5 \pm 1.5$ m. To estimate the incident wavelength and the in-ice wavelength in the NBB experiment, for
210 which no direct measurements were made, we revert to the first order linear Kelvin ship wake theory (Thomson, 1887). This theory states that the wavelength generated by point source moving in a straight line at a speed U is

$$\lambda^* = \frac{2\pi U^2}{g} \cos^2 \vartheta \quad (1)$$

where ϑ is the wave angle with respect to the ship heading and g is the gravitational acceleration. Waves generated from a moving ship can have any angle between 0 and 90° but waves of maximum amplitude (a_{max}) propagate at an angle of
215 $\vartheta|_{a_{\text{max}}} = \sin^{-1}(1/\sqrt{3}) \simeq 35.26^\circ$ (Soomere, 2007). Since this value is within the uncertainty range of our measurement in the GSL we use this angle for the computation of the incident wavelength for both experiments are thus $\lambda_{\text{GSL}}^* = 22.4$ m and $\lambda_{\text{NBB}}^* = 29.9$ m. Using the deep water dispersion relation, the wave periods are then valued to $T_{\text{GSL}} = 3.8$ s and $T_{\text{NBB}} = 4.4$ s. These values are going to be useful later in the discussion. Note that for this theory to apply it requires that the sea state is stationary and that the ship speed is constant, which is the case in both experiments.

220 Figure 5 shows snapshots of wave-induced break-up in the GSL experiment. Flexure-induced cracks are parallel to the wave phase plane, which propagates at an angle of $37^\circ \pm 5$ with respect to the ship heading. The three colored curves on figure 6 show the position of the furthest crack along the corresponding line shown on Figure 5 as a function of time. The break-up speed is obtained as the mean slope of the three linear regression, with a 95% confidence interval, and is 1.86 ± 0.04 m s $^{-1}$. This value is approximately 2.5 times slower than the measured wave phase speed $c_p = \lambda/T \simeq 5.0 \pm 0.8$ m s $^{-1}$.

Table 1. Wave and ice parameter values measured, estimated or calculated for both experiments, with associated uncertainties. Values in parentheses indicate extreme values whenever they are not equidistant from the mean.

Parameter	Symbol	GSL	NBB
Ship speed	U	$7.24 \pm 0.08 \text{ m s}^{-1}$	$8.35 \pm 0.05 \text{ m s}^{-1}$
Wave period	T	$4.0 \pm 0.2 \text{ s}$	$4.4 \pm 0.2 \text{ s}^{[a]}$
Incident wavelength	λ^*	$22.4 \pm 0.5 \text{ m}^{[b]}$	$29.9 \pm 0.5 \text{ m}^{[b]}$
In-ice wavelength	λ	$19.5 \pm 1.5 \text{ m}$	$24.2 \pm 1.4 \text{ m}^{[c]}$
Ice floe thickness	h	$0.3 \pm 0.1 \text{ m}$	$0.5 \pm 0.1 \text{ m}$
Air temperature	T_{air}	$-7.2 \text{ }^\circ\text{C}$	$+4.9 \text{ }^\circ\text{C}$
Ice temperature	T_{ice}	$-7 \pm 2 \text{ }^\circ\text{C}$	$-3 \pm 1 \text{ }^\circ\text{C}$
Ice salinity	S_{ice}	5 ± 1	3 ± 1
Brine volume	v_b	$0.04 (0.02, 0.06)$	$0.06 (0.03, 0.10)$
Break-up extent	L_{MIZ}	60 m	$> 560 \text{ m}$

^a Estimated using the Kelvin theory Eq. (1) and the deep water dispersion relation $\omega^2 = gk$.

^b Estimated using Eq. (1) with $\vartheta|_{\alpha_{\text{max}}}$ and respective ship speeds U .

^c Estimated using the mass loading dispersion relation Eq. (16).

225 In the GSL, the ice fractured up to 60 m from the ice edge leading to a partial break-up of the floe. In the NBB experiment, the 540 m-wide floe was completely broken up by the ship-generated waves. Figure 7 shows the breakup that has been captured by the UAV shortly after the passage of the ship (parallel to the horizontal axis of the of the image) in the GSL. Figure 8 shows only a part of the broken-up floe in NBB, where the floe was too large to be mapped entirely. In both images, one can distinguish that the largest floes have a preferential size, that the crack pattern is quite homogeneous and that floes have various sizes and
230 shapes with sharp corners. Those are clear signs indicating that they have been broken-up by the bending of surface waves.

4.2 FSD as a number density

To quantify the morphology of sea ice floes, the floe size distribution is first computed using the number density as it is done in most studies for decades (e.g. Rothrock and Thorndike, 1984; Toyota et al., 2006; Herman et al., 2021). The metric used as the floe size is the minor axis d since it is a good approximation of the distance between cracks which represents the linear
235 length scale generated by the breakup (Herman et al., 2018). To build the distribution, we first determine a certain number M of size categories d_i , $i = 1 \dots M$. To make sure that the result remains independent of the binning, we follow the normalization proposed by Stern et al. (2018) and set the number of bins $M = \sqrt{N}$, N being the total number of floes. The constant bin width Δd is set equal to the size range divided by the number of bins, i.e. $\Delta d = (d_{\text{max}} - d_{\text{min}})/M$. The probability density function computed from the number density, referred to as the NFSD, is then given by

$$240 \quad P_N(d_i) = \frac{n_i}{N\Delta d}, \quad \sum_{i=1}^M P_N(d_i)\Delta d = 1, \quad (2)$$

Figure 9 shows the NFSDs resulting from both experiments. The GSL NFSD exhibits a modal shape with a mean value of 2.8 m and a standard deviation of 1.2 m. The NBB NFSD on the other hand has a bimodal shape with a mean value of 5.9 m and a standard deviation of 3.4 m. It is interesting to see that the NBB FSD as a shape similar to what Herman et al. (2018) obtained in a laboratory wave-induced ice fracture experiment (more precisely in their test A 2060), which was interpreted as the sum of a power-law and a Gaussian distribution. However, when looking at Figs. 7 and 8, one can see that the area is mostly covered by large floes of similar size and a large number of very small ice fragments filling the cracks between the larger floes. The underestimation of the probabilities of finding a large floe in Fig. 8 comes from the fact that the NFSD weighs each floe equally, whereas a visual assessment puts more weight on larger floes because they cover a larger portion of the image than small floes.

4.3 Using the partial aerial concentration to compute the FSD

Let A be the total area covered by ice floes such that $A = \sum_{k=1}^N a_k$, with a_k the area of floe $k = 1, \dots, N$. Here, we consider that the probability for a given ice pixel in the image to belong to floe k to be directly related its the partial aerial concentration a_k/A . Hence, the bigger the floe, the higher the probability. Following the same procedure as for the number-based PDF for the binning, the probabilities are obtained by

$$P_A(d_i) = \frac{1}{\Delta d} \sum_{j=1}^{n_i} \frac{a_j}{A}, \quad \sum_i P_A(d_i) \Delta d = 1, \quad (3)$$

where a_j is the area of the j^{th} floe belonging to the i^{th} size bin. This representation, which we call the AFSD, is not only compatible with a visual evaluation of an arrangement of flat plates on a surface, it is also compatible with the definition of the ice thickness distribution (ITD) that is widely used in sea ice models to characterize the state of the ice cover over a given area (Hunke and Lipscomb, 2010). More recently, the FSD has also been defined that way in a large-scale coupled wave-ice model (Boutin et al., 2020). Using this approach to build the FSD thus makes its shape directly translatable from observations to models like the one of Boutin et al. (2020), which, at the moment, used the NSFSD shape since it is the only available from observations. Unfortunately, using the minor axis as the floe size implies that information on the floe shapes is lost. Hence, computing the total area of sea ice from the NFSD is bound to be non conservative and dependent on the assumed floe shape, problem which is solved by using the AFSD.

Figure 10 shows the AFSD for both experiments. By comparing the right panels of Figures 9 and 10 to Figure 8, it is clear that the AFSD is more coherent with what can be seen in orthomosaic than the NFSD does. The modal floe size for the GSL experiment is slightly shifted towards larger values with the AFSD (Fig. 10) compared to the NFSD (Fig. 9). It is worth noting here that the AFSD is much more robust to segmentation errors than the NFSD, since small artifact floes generated during the segmentation process are given a much smaller weight.

There are very few reports in the literature on wave-induced sea ice break-up events, and even fewer that are observed at adequate time and spatial scales. The two experiments presented here, carried out in two contrasting sets of environmental conditions, shed light on multiple aspects of wave-ice interactions: 1) the floe size distribution that results from wave-induced break-up, 2) wave propagation in sea ice and 3) wave attenuation, all of which are discussed below.

275 **5.1 Wave-induced floe size distribution**

The AFSDs obtained in this study (Figure 10) follow modal distributions, meaning that a preferential size results from wave-induced sea ice breakup, thus confirming what was obtained by process-based modelling studies (e.g. Fox and Squire, 1991; Herman, 2017; Montiel and Squire, 2017; Mokus and Montiel, 2021) and what was anecdotally reported by Squire (1995). The shape of the AFSDs also highlights the fact that this process alone does not explain the power law distributions observed at a larger scale where sea ice is potentially influenced by many different mechanisms and events. Additionally, the mean value \bar{d} of the AFSD increases with thickness: $\bar{d}_{\text{GSL}} = 3.57$ m with $h_{\text{GSL}} \in [10, 30]$ cm, while to $\bar{d}_{\text{NBB}} = 9.00$ m with $h_{\text{NBB}} \in [40, 60]$ cm, suggesting, like in a number of previous studies (e.g. Fox and Squire, 1991; Squire, 1995; Herman, 2017), that the preferential floe size obtained from wave-induced sea ice break-up is influenced by sea ice thickness. Another quantity associated with the FSD that is often used as a state variable in wave-ice interaction modeling studies (e.g. Dumont et al., 2011; Williams et al., 2013a; Bateson et al., 2020) is the maximum size d_{max} . Different theoretical frameworks have been proposed to relate the maximum size to a relevant physical length scale in the hope of identifying the underlying physical processes involved. Let's recall here the two main hypotheses there are in the literature.

The first hypothesis is the one used by Dumont et al. (2011) in their wave-ice interaction model. Their parameterization considered that the maximum floe size is the distance between two consecutive location of maximal flexural strain in a semi-infinite ice floe. In order to compute strains, they have assumed that sea ice is thin and homogeneous through its thickness so that it can be considered as an Euler-Bernoulli beam that conforms to a monochromatic sinusoidal wave described as $\eta(x, t) = a \sin(\omega t - kx)$. The flexural strain ε applied at a given time on the ice surface is therefore

$$\varepsilon = \frac{h}{2} \frac{\partial^2 \eta}{\partial x^2} = -\frac{ak^2 h}{2} \sin(kx - \omega t). \quad (4)$$

where ω is the wave angular frequency, k is the wavenumber, a its amplitude, and h the ice thickness. Taking the first-order derivative of Eq. (4) and setting it to zero gives the location of strain extrema, which are separated by a distance of $\lambda/2$ (Dumont et al., 2011). This approach assumes that the break-up occurs after a monochromatic wave has propagated into an unbroken ice plate, at many places within the ice plate simultaneously, and far from the stress-free edge.

Another theoretical framework that has been used in the last decade in the wave-ice interaction community (e.g. Toyota et al., 2011; Williams et al., 2013a; Herman, 2017; Boutin et al., 2018; Bateson et al., 2020) is the one described by Mellor (1983) based on Hétyenyi (1946), in which he derives an analytical solution for the position x^* of the maximum bending moment in

a beam subject to a downward force at its edge. Since an arithmetic error is present in the derivation made by Mellor (1983), which was briefly underlined by Boutin et al. (2018), we deemed important to recall the derivation of x^* .

305 First, Hétyenyi (1946) considers a semi-infinite Euler-Bernoulli beam of uniform thickness h that extends along the x -axis. When submitted to a load P acting downwards at its edge, a vertical deflection of the edge is generated and imposes a bending moment M along the beam defined as

$$M = -EI \frac{\partial^2 \eta}{\partial x^2}, \quad (5)$$

where E and I are respectively the elastic modulus and the second moment of area of the beam, i.e. its massless inertia (Hétyenyi, 1946). Considering a stress-free condition at the edge and that M vanishes for large x , the general solution is

$$M = -\frac{P}{\mu} e^{-\mu x} \sin \mu x, \quad \mu = \left(\frac{k_f}{4EI} \right)^{\frac{1}{4}}, \quad (6)$$

310 where k_f is the foundation modulus, which can be viewed as a Hooke's constant, and x is the axial direction of the beam (Hétyenyi, 1946). Setting the first-order derivative of Eq. (6) with respect to x to zero, we obtain the following algebraic equation :

$$e^{-\mu x} (\cos \mu x - \sin \mu x) = 0, \quad (7)$$

315 which is satisfied when $x \rightarrow \infty$ or when $x = (4n + 1)\pi/4\mu$ with $n = 0, 1, 2, \dots$. This implies that the location of the maximum bending moment, and therefore of maximal deformation, is

$$x^* = \frac{\pi}{4} \left(\frac{4EI}{k_f} \right)^{1/4}. \quad (8)$$

Even though x^* is derived for an Euler-Bernoulli beam, the second moment of area I of a Kirchoff-Love plate is used and the Young's modulus, noted Y , is set to be equivalent to the elastic modulus E of the plate. That way, we have

$$E = Y, \quad I = \frac{h^3}{12(1 - \nu^2)} \quad (9)$$

320 which implies that

$$x^* = \frac{\pi}{4} \left(\frac{Y^* h^3}{3\rho_w g (1 - \nu^2)} \right)^{1/4}. \quad (10)$$

where $\nu = 0.3$ the Poisson ratio, $\rho_w \simeq 1025 \text{ kg m}^{-3}$ the sea water density and g the gravitational acceleration. Another consideration made here is that, in order to take into account for the fact that the plate lies on water, the foundation modulus was set to $\rho_w g$.

325 Mellor (1983) used this framework for determining a flexure-induced fracture distance in the context of ice rafting, not for the case of wave-induced breakup. He wrote that "*when the ice is flexed, it will tend to break first at a distance x^* from the free edge*". This comment has led numerous wave-ice interaction studies, namely Toyota et al. (2011), to consider that

x^* is "the minimum ice length at which breakup will occur due to flexure stress", Williams et al. (2013a) to interpret x^* as "[corresponding] to the diameter below which flexural failure cannot occur" and Boutin et al. (2018) to assume x^* is the diameter "below which [...] no flexural failure is possible". But, since WIMs use $\lambda/2$ as d_{\max} based on the fact that sea ice will break at extrema of deformation, shouldn't x^* be also considered as a maximum floe length scale since it is based upon the same mathematical premise ?

In order to compute x^* and compare this length scale with the observed maximum floe sizes, it is necessary to estimate the effective Young's modulus. Estimations of Young's modulus in wave-ice interaction studies (e.g. Williams et al., 2013a) are commonly based on empirical relationships. For Young's modulus, Timco and Weeks (2010) obtained

$$Y = Y_0(1 - 3.51v_b) \quad (11)$$

where $Y_0 \simeq 10$ GPa and v_b is the brine volume. As argued by Williams et al. (2013a), an effective value of $Y^* = Y - 0.5$ GPa must be used when a cyclic loading of a period less than 10 s is considered. Y^* might thus be used for calculating the flexural rigidity length scale x^* since waves in our experiments had a period lower than 10 seconds. The brine volume depends on ice salinity, but even more strongly on ice temperature. The warmer the ice, the larger the brine volume and the porosity are. Here we use the empirical relationship of Cox and Weeks (1983) to estimate v_b , which is

$$v_b = \frac{\rho_{\text{ice}} S}{F} \quad \text{with} \quad (12)$$

$$F = \begin{cases} -4.732 - 22.45 T_{\text{ice}} - 0.6397 T_{\text{ice}}^2 - 0.01074 T_{\text{ice}}^3 & \text{for } -2^\circ\text{C} \geq T_{\text{ice}} \geq -22.9^\circ\text{C} \\ 9899 + 1309 T_{\text{ice}} + 55.27 T_{\text{ice}}^2 + 0.716 T_{\text{ice}}^3 & \text{for } -22.9^\circ\text{C} > T_{\text{ice}} > -30^\circ\text{C} \end{cases} \quad (13)$$

Unfortunately, the salinity of the ice was not measured during the experiments. To estimate it, we revert to the empirical study of Cox and Weeks (1974) who showed that thin and cold young ice has a typical salinity around 5 ppt, while warm sea ice at the end of the melt season can have as low as 2 ppt. We thus set $S_{\text{GSL}} = 5 \pm 1$ and $S_{\text{NBB}} = 3 \pm 1$ to account for the two different situations as well as the uncertainty associated to these estimates. The ice temperature is set close to the freezing point of sea water for NBB, and close to the air temperature for GSL (see Table 1). This gives $v_b = 0.04$ (0.02, 0.06) for GSL and $v_b = 0.06$ (0.03, 0.10), with extrema values shown in parentheses. Using Eq. (11) with these parameter values, the maximum and minimum values for the effective Young's modulus values in the GSL experiment are $[Y_{\min}^*, Y_{\max}^*] = [7.93, 9.23]$ GPa and are $[Y_{\min}^*, Y_{\max}^*] = [6.56, 8.85]$ GPa in the NBB. Given these value intervals for Young's modulus and the thickness estimation and measurement made respectively for the GSL and the NBB, it is possible to compute x^* for both experiment (see Table 2).

It is worth mentioning that it is by using a quasi-static framework that Mellor (1983) obtained x^* and, since wave-induced sea ice breakup is inherently dynamic, we wonder if x^* is an appropriate scale for the phenomenon under study. Tkacheva (2001), on the other hand, studied the diffraction of a plane wave by a semi-infinite plate and focuses on quantities relevant to the context of wave-induced breakup, namely the transmission coefficient and the position of maximum strain relative to wave and ice properties. One key quantity introduced in Tkacheva (2001) is the dimensionless reduced rigidity β mathematically

expressed as

$$\beta = \frac{16\pi^4 EI}{\rho_w g \lambda^4}. \quad (14)$$

360 This quantity arises from the dimensional analysis of the the boundary conditions considered for solving the velocity potential of a plane wave being diffracted by a plate. It translates to

$$\beta = \frac{4\pi^4 Y h^3}{3(1 - \nu^2)\rho_w g \lambda^4} \quad (15)$$

under the Kirchoff-Love plate approximation and when assuming that the elastic modulus is equal to Young's modulus. Computing β with the reference values of Young's modulus derived from Timco and Weeks (2010), the incident wavelengths and
 365 the ice thicknesses estimated for the two experiments gives $\beta_{\text{GSL}} \in [0.4, 14.0]$ $\beta_{\text{NBB}} \in [7.5, 33.9]$. which translate to transmission coefficients $|T|_{\text{GSL}} \in [0.6, 0.4]$ and $|T|_{\text{NBB}} \in [0.5, 0.4]$ (see Fig. 2 of Tkacheva, 2001). These values are contradictory of what was observed, that is a near perfect transmission of the ship waves into the ice plate. This contradiction can either come from a bad estimation of the ice thickness, the incident wavelength or Young's modulus. Despite the uncertainties, thickness and wavelength have been measured and estimated, and do not allow for lower values of β . Young's modulus on the other
 370 hand have been estimated from empirical relationships that might not be applicable to the sampled sea ice, which was grey, grey-white ice in the GSL and heavily rotten first-year ice in NBB. Also, the way waves propagated through sea ice, with the in-ice wavelength smaller than the incident wavelength (see Table 1), suggests that its elasticity is very low. An alternative method to quantify Y may thus be used in order to see if x^* represents adequately d_{max} .

Tkacheva (2001) also computed the position of maximum strain, expressed as a fraction of the incident wavelength, as a
 375 function of β (see Fig. 7 of Tkacheva, 2001). Since d_{max} has been derived from the position of maximum strain in both Mellor (1983) and Dumont et al. (2011), we can translate this way of thinking with Tkacheva (2001) and obtain a value of β by measuring the maximal size and dividing it by the incident wavelength. Table 2 displays values of d_{max}/λ , which amounts to 0.31 for the GSL and 0.52 for the NBB. These values lead to $\beta_{\text{GSL}} \sim 7.5 \times 10^{-3}$ and $\beta_{\text{NBB}} \sim 2.5 \times 10^{-2}$ to transmission coefficients of over 95 % according to the derivation made Tkacheva (2001). We dismiss the possible value of $\beta_{\text{NBB}} > 10^0$
 380 since it corresponds to situations where more than 50 % of the incident wave would have been reflected.

With values of β , thickness and wavelength for each experiment, it is possible to estimate Young's modulus by inverting Eq. (15). Doing so we obtain $Y_{\text{GSL}} \in [5, 130] \times 10^6$ Pa and $Y_{\text{NBB}} \in [7, 22] \times 10^6$ Pa, with the lower (upper) bound corresponding the highest (lowest) thickness value, values that are 1 to 4 orders of magnitude smaller than what is obtained from empirical relationships (see Table 2). Using these values to compute x^* as an indicator for d_{max} does not fit with observations. This
 385 suggests that the quasi-static theoretical framework of Mellor (1983) does not grasp the underlying physics of wave-induced sea ice breakup. In our opinion, it should also be considered as a coincidence that x^* is close to the minimal size in Fig. 10 since it should in principle represent a maximum size.

Tkacheva (2001) provides interesting information relating the position of maximum strain, hence d_{max} , to the sea ice rigidity and incident wavelength. But, since many models obtain modal shaped FSDs by assuming that sea ice breaks up at the position
 390 where ε_c is reached, this quantity may be tied to the preferential size. Relating ε_c and the maximum strain to β might allow to

Table 2. Physical quantities related to the AFSDs and comparison to x^* with different approaches to estimate sea ice Young’s modulus.

Exp.	h	\bar{d}	d_{mode}	d_{max}	d_{max}/λ^*	Ref.	β	Y	x^*
	cm	m	m	m	-			Pa	m
GSL	20 ± 10	3.7	4.1	7.0	0.31	Timco and Weeks (2010)		$[7.93, 9.23] \times 10^9$	[3.3, 7.5]
						Tkacheva (2001)	$\sim 7.5 \times 10^{-3}$	$[130, 5] \times 10^6$	1.2
NBB	50 ± 10	8.7	7.8	15.5	0.52	Timco and Weeks (2010)		$[6.56, 8.85] \times 10^9$	[9.1, 12.3]
						Tkacheva (2001)	$\sim 2.5 \times 10^{-2}$	$[22, 7] \times 10^6$	2.1

parametrize the wave-induced FSD with the physical properties of waves and ice but also to identify where does the preferential size come from.

5.2 Break-up evolution and wave propagation

In the two experiments, ice broke-up from the edge inward with the furthest crack at a given time oriented parallel to the wave phase plane. The speed c_b at which the break-up progressed could only be measured in the GSL experiment using the UAV footage.

Figure 11 a) and b) respectively show the phase speed and the group-to-phase speed ratio relative to the wavenumber. Along with the data of the GSL experiment, ice-free deep water waves and two regimes of waves-in-ice, namely flexural waves traveling in a thin elastic plate and waves affected by the inertia of a floating material, obeying the so-called *mass loading* dispersion relation, are presented in Figure 11. The general dispersion relation that describes these two regimes is given by (Liu and Mollo-Christensen, 1988)

$$\omega^2 = \left(gk + \frac{Yh^3k^5}{12(1-\nu^2)\rho_w} \right) \left(1 + \frac{\rho_i hk}{\rho_w} \right)^{-1}. \quad (16)$$

Figure 11a shows that the measured phase speed of the wave propagating into the unbroken ice $c_p \simeq 4.95 \pm 0.75 \text{ m s}^{-1}$ is lower than both the phase speed of deep water and inertial-gravity waves but still within their range due to uncertainty. This result suggest that waves responsible for the break-up, which are visible from the UAV footage, could propagate following the mass loading dispersion relation. This observation would be consistent with what Sutherland and Dumont (2018) observed in brash ice. This observation supports also supports the idea that the effective Young’s modulus of the ice encountered in both experiments might have been low as was suggested in sec 5.1. Figure 11b shows that break-up speed $c_b \simeq 1.86 \pm 0.04 \text{ m s}^{-1}$ is lower than the speed of inertial-gravity waves-in-ice $c_g \simeq 2.1 \pm 0.2 \text{ m s}^{-1}$, but still within the uncertainty.

From the video footage of the GSL experiment, we can clearly see that waves were attenuated along their propagation into the ice. Since attenuation reduces the wave amplitude, it would contribute to slow down the break up process and hence lead to c_b being smaller than c_g . On the other hand, it is also possible that the leading waves of the group might fatigue the ice and lower the critical strain Langhorne et al. (1998), thus increasing the breakup speed. Observing that $c_b \leq c_g$ suggest that attenuation has had more of an influence than fatigue in the GSL experiment.

415 The results presented here allow for a rough analysis of the wave propagation into the ice, but there is clearly a need for more experiments where wave propagation is measured adequately measured. Not only would this provide data to help identify the dispersion relation of wave propagating into ice but also to quantify the respective contributions of attenuation and fatigue to the breakup speed.

5.3 Break-up extent and wave energy attenuation

420 In the GSL, the break-up extent reached 60 m from the original floe edge. In the NBB experiment the entire floe that was approximately 540 m wide broke-up. Assuming that the incident waves were similar in terms of period, wavelength and amplitude for both experiments (see Table 1), this suggests that the wave attenuation rate was higher (up to one order of magnitude) for thinner ice than for thicker ice. This might be a counter-intuitive result in regards to proposed theories for wave attenuation. Far from criticizing these theories, that are meant to be applied at large scale where waves experience averaged
425 ice properties, this result rather suggest that wave energy dissipation or scattering depends on material properties that are not considered by models (e.g. ice porosity, temperature, heterogeneity, composition, rigidity) and often not carefully measured in field experiments.

6 Conclusions

Results obtained from the analysis of two wave-induced sea ice break-up experiments, captured by an unmanned aerial vehicle
430 and carried out in two contrasting sets of environmental conditions, provide direct and detailed measurements that shed light on many aspects related to wave-ice interactions. The aerial imagery of the break-up event also allowed the characterization of wave propagation, break-up evolution and extent.

A novel way of computing the FSD, that is using the partial aerial concentration rather than the number density, is proposed. The AFSD allows mass conservation since the total sea ice area can be calculated from it, something that cannot be achieved
435 using the NFSD without depending on the assumed shape of the floes. We thus deem the AFSD to be physically more relevant than the NFSD. It is also fully coherent with numerical modeling frameworks that solve for the evolution of conserved quantities such as the ITD. The AFSD also allows to identify the presence of a preferential floe size as a result of wave-induced break-up events. The observation of a preferential size, along with the fact that ice thickness has an effect on it, resonates with many other process-based modeling studies and anecdotal evidences reported in the literature (e.g. Fox and Squire, 1991; Squire,
440 1995; Kohout et al., 2016b; Herman, 2017).

Theoretical frameworks relating the position of maximal strain to the incident wavelength (Dumont et al., 2011), to sea ice flexural rigidity (Mellor, 1983) or to both these quantities (Tkacheva, 2001) were compared against the observed AFSDs. In the end, the maximal floe size seems to be controlled by both incident wavelength and sea ice rigidity.

The estimation of the Young's modulus of the sea ice encountered during the experiments was first made by using the
445 empirical relationships of Cox and Weeks (1974), Cox and Weeks (1983) and Timco and Weeks (2010). The computed values lead to an underestimation of the transmission coefficient given by Tkacheva (2001) and were thus considered to be wrong

estimates. Alternatively, the computation of the dimensionless rigidity β introduced by Tkacheva (2001) from the ratio between the observed maximal size d_{\max} and the incident wavelength λ^* lead to Young's modulus values that were not only orders of magnitude lower than the earlier estimates but that also lead to transmission coefficients which were coherent with our observations. Quantification of the transmission coefficient via the measurement of the amplitudes of both the incident and in-ice waves in further experiments would allow for a better assessment of the applicability of the theoretical framework of Tkacheva (2001) in a real situation. Moreover, the development of theoretical framework relating the location of the critical strain to wave and ice properties and the empirical identification of the critical strain are key in order to understand the physics causing a preferential size to arise from wave-induced sea breakup.

It was also identified that waves propagating into the unbroken ice might follow the mass loading dispersion relation since the wavelength and the phase speed were smaller in unbroken ice than in deep water. Moreover, the break-up speed in the GSL experiment is less or equal to the group speed of inertial-gravity waves, thus suggesting that attenuation played a bigger role than ice fatigue during the process. Finally, waves were attenuated much faster in the thinner ice floe. However, the lack of in situ data about sea ice properties and wave characteristics over the course of their propagation does not allow us to identify the processes at play or to partition the contributions of the different processes expected to attenuate waves in ice. In the end, these results show that using a ship to generate waves allows carrying experiment in a controlled yet natural environment. This is a promising way to study wave-induced sea ice break-up which advances our understanding of numerous wave-ice interactions. Collecting key in situ data to complement the UAV would significantly improve the scientific output. It could be done by using ice-going platforms such as an ice canoe to deploy wave buoys and measure ice properties (thickness, temperature, salinity, snow cover), as was done by Sutherland and Dumont (2018).

Code and data availability. The code and data required to produce the results are available on demand at the following git repository: <https://gitlasso.uqar.ca/dumael02/breakup>.

Video supplement. The video of the GSL experiment is available on ResearchGate at the following <https://doi.org/10.13140/RG.2.2.32873.62564> under a CC BY-NC-ND 4.0 license.

Author contributions. EDL planned and conducted both experiments, developed the image processing tools, performed the data analysis, wrote the first draft of the paper and participated to the discussion and writing. DD provided the original idea for the experiment, provided guidance in data analysis, and participated to the discussion and writing.

Competing interests. The authors declare that they have no conflict of interest.

Acknowledgements. The authors would like to thank Tim Williams and one anonymous reviewer for their careful reading and for sharing
475 valuable insight that helped improved the manuscript. We also thank the Canadian Coast Guard crew of the icebreaker *Amdunsen* for their support and collaboration in carrying out both experiments opportunistically. This work was financially supported by the NSERC Discovery Grant to DD *Physics of Seasonal Sea Ice* (RGPIN-2019-06563, RGPAS-2019-00068), the Odyssee Saint-Laurent program of the Réseau Québec maritime and by the Canadian Foundation for Innovation and Amundsen Science. This research contributes to the scientific program Québec-Océan.

480 **References**

- Alberello, A., Onorato, M., Bennetts, L., Vichi, M., Eayrs, C., Machutchon, K., and Toffoli, A.: Brief communication: Pancake ice floe size distribution during the winter expansion of the Antarctic marginal ice zone, *Cryosphere*, 13, 41–48, <https://doi.org/10.5194/tc-13-41-2019>, 2019.
- Bateson, A. W., Feltham, D. L., Schröder, D., Hosekova, L., Ridley, J. K., and Aksenov, Y.: Impact of floe size distribution on seasonal
485 fragmentation and melt of Arctic sea ice, *The Cryosphere Discussions*, <https://doi.org/10.5194/tc-2019-44>, 2020.
- Bennetts, L. G., Peter, M. A., Squire, V. A., and Meylan, M. H.: A three-dimensional model of wave attenuation in the marginal ice zone, *Journal of Geophysical Research: Oceans*, 115, <https://doi.org/10.1029/2009JC005982>, 2010.
- Bennetts, L. G., O'Farrell, S., and Uotila, P.: Brief communication: Impacts of ocean-wave-induced breakup of Antarctic sea ice via thermodynamics in a stand-alone version of the CICE sea-ice model, *Cryosphere*, <https://doi.org/10.5194/tc-11-1035-2017>, 2017.
- 490 Boutin, G., Ardhuin, F., Dumont, D., Sévigny, C., Girard-Ardhuin, F., and Accensi, M.: Floe Size Effect on Wave-Ice Interactions: Possible Effects, Implementation in Wave Model, and Evaluation, *Journal of Geophysical Research: Oceans*, 123, 4779–4805, <https://doi.org/10.1029/2017JC013622>, 2018.
- Boutin, G., Lique, C., Ardhuin, F., Talandier, C., Accensi, M., Girard-Ardhuin, F., and Rousset, C.: Towards a coupled model to investigate wave-sea ice interactions in the Arctic marginal ice zone, *Cryosphere*, 14, <https://doi.org/10.5194/tc-14-709-2020>, 2020.
- 495 Casas-Prat, M. and Wang, X. L.: Projections of Extreme Ocean Waves in the Arctic and Potential Implications for Coastal Inundation and Erosion, *Journal of Geophysical Research: Oceans*, <https://doi.org/10.1029/2019JC015745>, 2020.
- Cavaliere, D. J. and Parkinson, C. L.: Arctic sea ice variability and trends, 1979-2010, *The Cryosphere*, 6, 881, 2012.
- Comiso, J. C., Parkinson, C. L., Gersten, R., and Stock, L.: Accelerated decline in the Arctic sea ice cover, *Geophysical Research Letters*, <https://doi.org/10.1029/2007GL031972>, 2008.
- 500 Cox, G. and Weeks, W.: Equations for Determining the Gas and Brine Volumes in Sea-Ice Samples, *J. Glaciol.*, 29, 306–316, <https://doi.org/doi:10.3189/S0022143000008364>, 1983.
- Cox, G. F. N. and Weeks, W. F.: Salinity Variations in Sea Ice, *J. Glaciol.*, 13, 109–120, <https://doi.org/10.3189/S0022143000023418>, 1974.
- Dumont, D., Kohout, A., and Bertino, L.: A wave-based model for the marginal ice zone including a floe breaking parameterization, *Journal of Geophysical Research: Oceans*, 116, 2011.
- 505 Fox, C. and Squire, V. A.: Strain in shore fast ice due to incoming ocean waves and swell, *Journal of Geophysical Research*, <https://doi.org/10.1029/90jc02270>, 1991.
- Guimarães, P. V., Ardhuin, F., Sutherland, P., Accensi, M., Hamon, M., Pérignon, Y., Thomson, J., Benetazzo, A., and Ferrant, P.: A surface kinematics buoy (SKIB) for wave-current interaction studies, *Ocean Science*, 14, <https://doi.org/10.5194/os-14-1449-2018>, 2018.
- Herman, A.: Sea-ice floe-size distribution in the context of spontaneous scaling emergence in stochastic systems, *Physical Review E*, 81,
510 66 123, 2010.
- Herman, A.: Wave-induced stress and breaking of sea ice in a coupled hydrodynamic discrete-element wave-ice model, *Cryosphere*, <https://doi.org/10.5194/tc-11-2711-2017>, 2017.
- Herman, A., Evers, K. U., and Reimer, N.: Floe-size distributions in laboratory ice broken by waves, *Cryosphere*, 12, 685–699, <https://doi.org/10.5194/tc-12-685-2018>, 2018.
- 515 Herman, A., Wenta, M., and Cheng, S.: Sizes and Shapes of Sea Ice Floes Broken by Waves – A Case Study From the East Antarctic Coast, *Frontiers Earth Sci.*, 9, 390, <https://doi.org/10.3389/feart.2021.655977>, 2021.

- Hétyenyi, M.: *Beams On Elastic Foundation Theory With Applications In The Fields Of Civil And Mechanical Engineering*, The University Of Michigan Press, 1946.
- 520 Holt, B. and Martin, S.: The effect of a storm on the 1992 summer sea ice cover of the Beaufort, Chukchi, and East Siberian Seas, *Journal of Geophysical Research: Oceans*, 106, 1017–1032, 2001.
- Horvat, C. and Tziperman, E.: A prognostic model of the sea-ice floe size and thickness distribution, *The Cryosphere*, 9, 2119–2134, 2015.
- Hunke, E. C. and Lipscomb, W. H.: *CICE : the Los Alamos Sea Ice Model Documentation and Software User ' s Manual LA-CC-06-012*, Research Report, pp. 1–76, <https://doi.org/10.1111/j.1523-1747.2003.12629.x>, 2010.
- 525 Kohout, A. L. and Meylan, M. H.: An elastic plate model for wave attenuation and ice floe breaking in the marginal ice zone, *Journal of Geophysical Research: Oceans*, 113, <https://doi.org/10.1029/2007JC004434>, 2008.
- Kohout, A. L., Williams, M. J., Dean, S. M., and Meylan, M. H.: Storm-induced sea-ice breakup and the implications for ice extent, *Nature*, <https://doi.org/10.1038/nature13262>, 2014.
- Kohout, A. L., Williams, M. J., Toyota, T., Lieser, J., and Hutchings, J.: In situ observations of wave-induced sea ice breakup, *Deep-Sea Research Part II: Topical Studies in Oceanography*, 131, <https://doi.org/10.1016/j.dsr2.2015.06.010>, 2016a.
- 530 Kohout, A. L., Williams, M. J. M., Toyota, T., Lieser, J., and Hutchings, J.: In situ observations of wave-induced sea ice breakup, *Deep Sea Research Part II: Topical Studies in Oceanography*, 131, 22–27, 2016b.
- Kwok, R. and Rothrock, D. A.: Decline in Arctic sea ice thickness from submarine and ICESat records: 1958–2008, *Geophysical Research Letters*, 36, 2009.
- 535 Langhorne, P. J., Squire, V. A., Fox, C., and Haskell, T. G.: Break-up of sea ice by ocean waves, *Annals of Glaciology*, <https://doi.org/10.3189/S0260305500017869>, 1998.
- Li, J., Ma, Y., Liu, Q., Zhang, W., and Guan, C.: Growth of wave height with retreating ice cover in the Arctic, *Cold Regions Science and Technology*, 164, <https://doi.org/10.1016/j.coldregions.2019.102790>, 2019.
- Liu, A. K. and Mollo-Christensen, E.: Wave Propagation in a Solid Ice Pack, *Journal of Physical Oceanography*, 18, [https://doi.org/10.1175/1520-0485\(1988\)018<1702:wpiasi>2.0.co;2](https://doi.org/10.1175/1520-0485(1988)018<1702:wpiasi>2.0.co;2), 1988.
- 540 Lu, P., Li, Z. J., Zhang, Z. H., and Dong, X. L.: Aerial observations of floe size distribution in the marginal ice zone of summer Prydz Bay, *Journal of Geophysical Research: Oceans*, 113, 2008.
- Mellor, M.: *Mechanical behavior of sea ice*, Cold regions research and engineering, 1983.
- Meyer, F.: Topographic distance and watershed lines, *Signal Processing*, 38, 113–125, [https://doi.org/10.1016/0165-1684\(94\)90060-4](https://doi.org/10.1016/0165-1684(94)90060-4), 1994.
- 545 Mokus, N. G. A. and Montiel, F.: Wave-triggered breakup in the marginal ice zone generates lognormal floe size distributions, *The Cryosphere Discussions*, 2021, 1–33, <https://doi.org/10.5194/tc-2021-391>, 2021.
- Montiel, F. and Squire, V. A.: Modelling wave-induced sea ice break-up in the marginal ice zone, *Proceedings of the Royal Society A: Mathematical, Physical and Engineering Sciences*, 473, <https://doi.org/10.1098/rspa.2017.0258>, 2017.
- Rinke, A., Maturilli, M., Graham, R. M., Matthes, H., Handorf, D., Cohen, L., Hudson, S. R., and Moore, J. C.: Extreme cyclone events in the Arctic: Wintertime variability and trends, *Environmental Research Letters*, <https://doi.org/10.1088/1748-9326/aa7def>, 2017.
- 550 Rothrock, D. A. and Thorndike, A. S.: Measuring the Sea Ice Floe Size Distribution., *Journal of Geophysical Research*, 89, 6477–6486, <https://doi.org/10.1029/JC089iC04p06477>, 1984.
- Smith, M. and Thomson, J.: Scaling observations of surface waves in the Beaufort Sea, *Elementa*, 2016, <https://doi.org/10.12952/journal.elementa.000097>, 2016.
- Soomere, T.: Nonlinear components of ship wake waves, *Applied Mechanics Reviews*, <https://doi.org/10.1115/1.2730847>, 2007.

- 555 Squire, V.: Of Ocean Waves and Sea Ice, *Annual Review of Fluid Mechanics*, <https://doi.org/10.1146/annurev.fluid.27.1.115>, 1995.
- Squire, V. A.: Of ocean waves and sea-ice revisited, <https://doi.org/10.1016/j.coldregions.2007.04.007>, 2007.
- Squire, V. A.: A fresh look at how ocean waves and sea ice interact, *Philosophical Transactions of the Royal Society A: Mathematical, Physical and Engineering Sciences*, 376, 20170342, 2018.
- Squire, V. A.: Ocean Wave Interactions with Sea Ice: A Reappraisal, *Annual Review of Fluid Mechanics*, 52, [https://doi.org/10.1146/annurev-](https://doi.org/10.1146/annurev-fluid-010719-060301)
560 [fluid-010719-060301](https://doi.org/10.1146/annurev-fluid-010719-060301), 2020.
- Steele, M.: Sea ice melting and floe geometry in a simple ice-ocean model, *Journal of Geophysical Research: Oceans*, 97, 17729–17738, 1992.
- Stern, H. L., Schweiger, A. J., Zhang, J., and Steele, M.: On reconciling disparate studies of the sea-ice floe size distribution, *Elementa*, <https://doi.org/10.1525/elementa.304>, 2018.
- 565 Stopa, J. E., Arduin, F., and Girard-Arduin, F.: Wave climate in the Arctic 1992-2014: Seasonality and trends, *Cryosphere*, 10, <https://doi.org/10.5194/tc-10-1605-2016>, 2016.
- Sutherland, P. and Dumont, D.: Marginal ice zone thickness and extent due to wave radiation stress, *Journal of Physical Oceanography*, 48, 1885–1901, <https://doi.org/10.1175/JPO-D-17-0167.1>, 2018.
- Thomson, J. and Rogers, W. E.: Swell and sea in the emerging Arctic Ocean, *Geophysical Research Letters*, 41, 3136–3140, 2014.
- 570 Thomson, W.: On Ship Waves, *Trans. Inst. Mech. Eng.*, 8, 409–433, 1887.
- Timco, G. W. and Weeks, W. F.: A review of the engineering properties of sea ice, *Cold Regions Science and Technology*, 60, 107–129, <https://doi.org/10.1016/j.coldregions.2009.10.003>, 2010.
- Tkacheva, L. A.: Surface Wave Diffraction on a Floating Elastic Plate, *Fluid Dynamics*, 36, 776–789, 2001.
- Toyota, T. and Enomoto, H.: Analysis of sea ice floes in the Sea of Okhotsk using ADEOS/AVNIR images, in: *Proceedings of the 16th IAHR International Symposium on Ice*, Dunedin, New Zealand, pp. 211–217, 2002.
- 575 Toyota, T., Takatsuji, S., and Nakayama, M.: Characteristics of sea ice floe size distribution in the seasonal ice zone, *Geophysical research letters*, 33, 2006.
- Toyota, T., Haas, C., and Tamura, T.: Size distribution and shape properties of relatively small sea-ice floes in the Antarctic marginal ice zone in late winter, *Deep Sea Research Part II: Topical Studies in Oceanography*, 58, 1182–1193, 2011.
- 580 Weeks, W. F., Tucker III, W. B., Frank, M., and Fungcharoen, S.: Characterization of surface roughness and floe geometry of Sea Ice over the Continental Shelves of the Beaufort and Chukchi Seas, in: *Symposium on Sea Ice Processes and Models*, vol. 2, pp. 32–41, 1980.
- Williams, T. D., Bennetts, L. G., Squire, V. A., Dumont, D., and Bertino, L.: Wave–ice interactions in the marginal ice zone. Part 1: Theoretical foundations, *Ocean Modelling*, 71, 81–91, 2013a.
- Williams, T. D., Bennetts, L. G., Squire, V. A., Dumont, D., and Bertino, L.: Wave–ice interactions in the marginal ice zone. Part 2: Numerical
585 [implementation and sensitivity studies along 1D transects of the ocean surface](https://doi.org/10.1016/j.oceanmod.2013.06.002), *Ocean Modelling*, 71, 92–101, 2013b.
- Zhang, J., Stern, H., Hwang, B., Schweiger, A., Steele, M., Stark, M., and Graber, H. C.: Modeling the seasonal evolution of the Arctic sea ice floe size distribution, *Elementa*, <https://doi.org/10.12952/journal.elementa.000126>, 2016.
- Zhang, Q. and Skjetne, R.: Image techniques for identifying sea-ice parameters, *Modeling, Identification and Control*, 35, 293–301, <https://doi.org/10.4173/mic.2014.4.6>, 2014.
- 590 Zhang, Q. and Skjetne, R.: Image processing for identification of sea-ice floes and the floe size distributions, *IEEE Transactions on Geoscience and Remote Sensing*, 53, 2913–2924, <https://doi.org/10.1109/TGRS.2014.2366640>, 2015.
- Zhang, Q. and Skjetne, R.: *Sea Ice Image Processing with MATLAB*, Taylor & Francis, 2018.

- Zhang, Q., Skjetne, R., Løset, S., and Marchenko, A.: Digital image processing for sea ice observations in support to arctic DP operations, in: Omae, Rio de Janeiro, 2012.
- 595 Zhang, Q., Skjetne, R., and Su, B.: Automatic image segmentation for boundary detection of apparently connected sea-ice floes, in: Proceedings of the International Conference on Port and Ocean Engineering under Arctic Conditions, POAC, 2012, 2013.

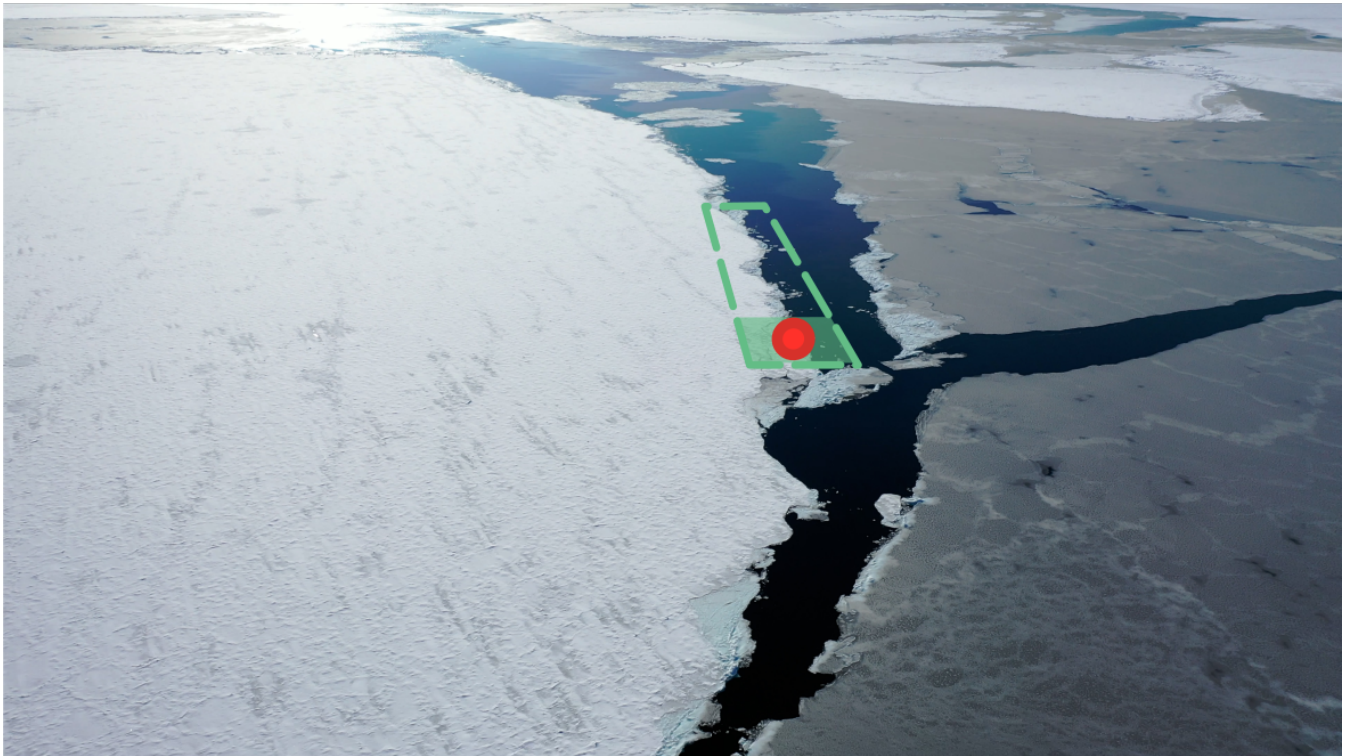
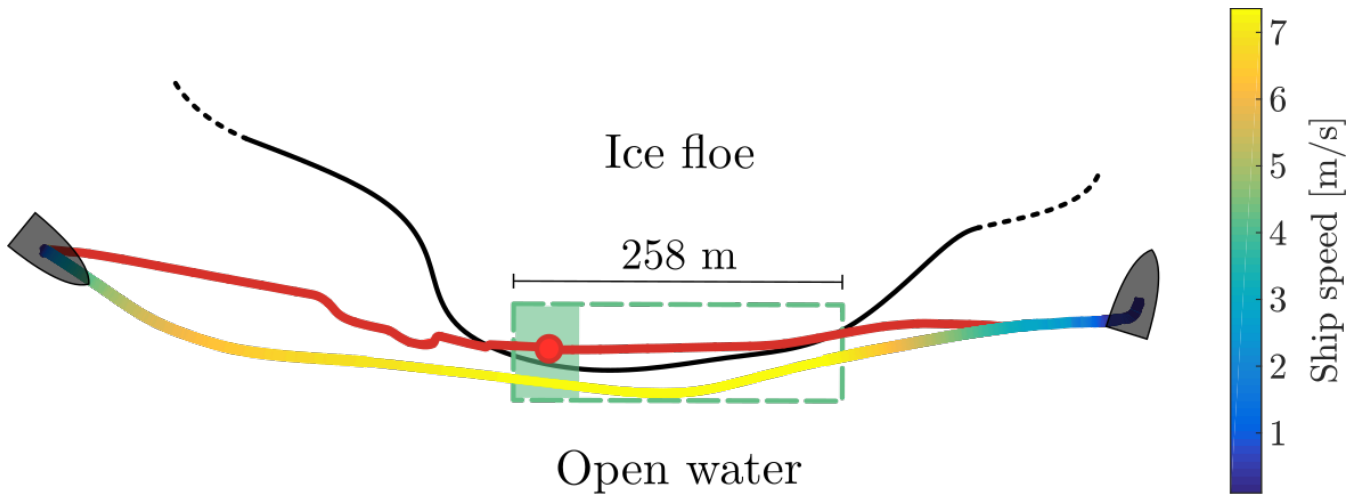


Figure 1. Schematic representation of the experiment conducted in the GSL. The grey shape represents the ship, while the red and blue-to-yellow lines are respectively the UAV and ship GPS tracks. The red dot is the position where the drone filmed the break-up from a fixed position, and the filled green rectangle is its field of view. The dashed green rectangle is the area covered by the panoramic picture obtained by taking multiple pictures of the resulting broken ice (Figure 7). The black line shows the approximate location of the floe edge. To the bottom is an overview image of the selected floe and surrounding ice conditions

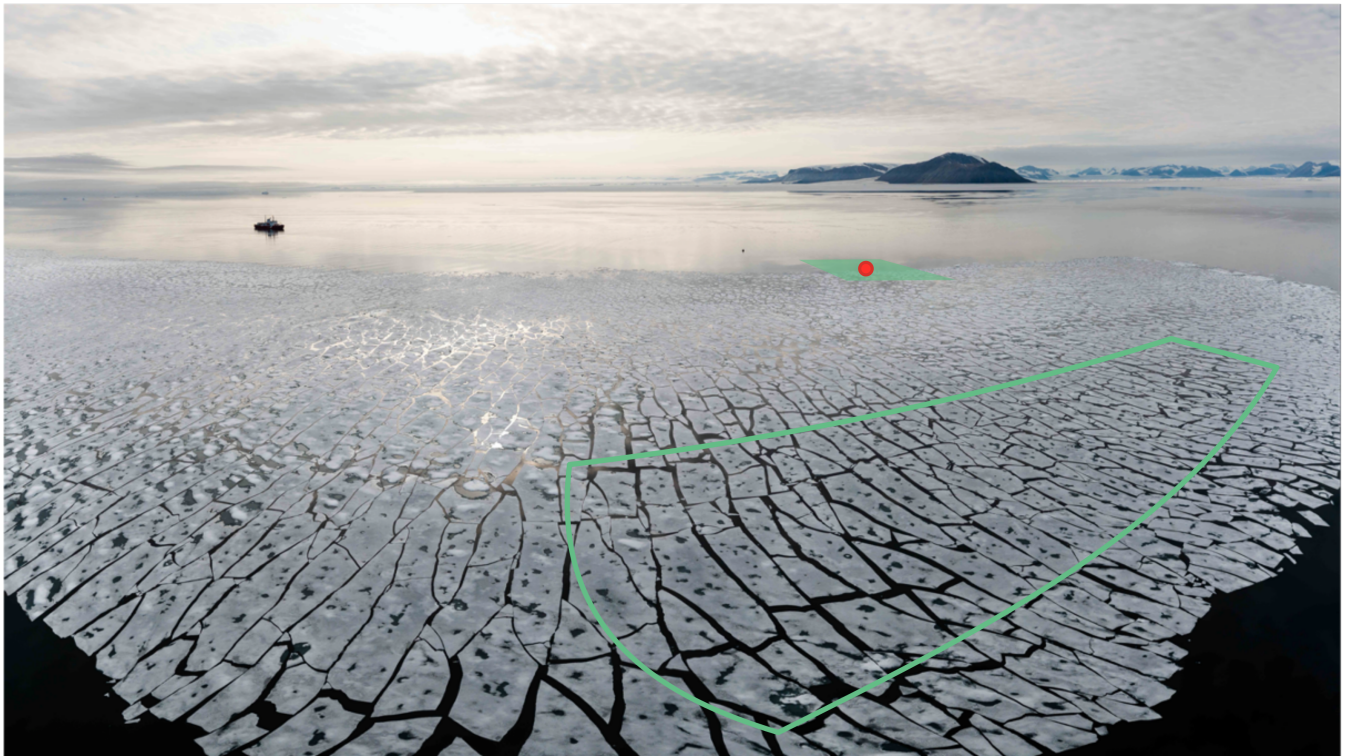
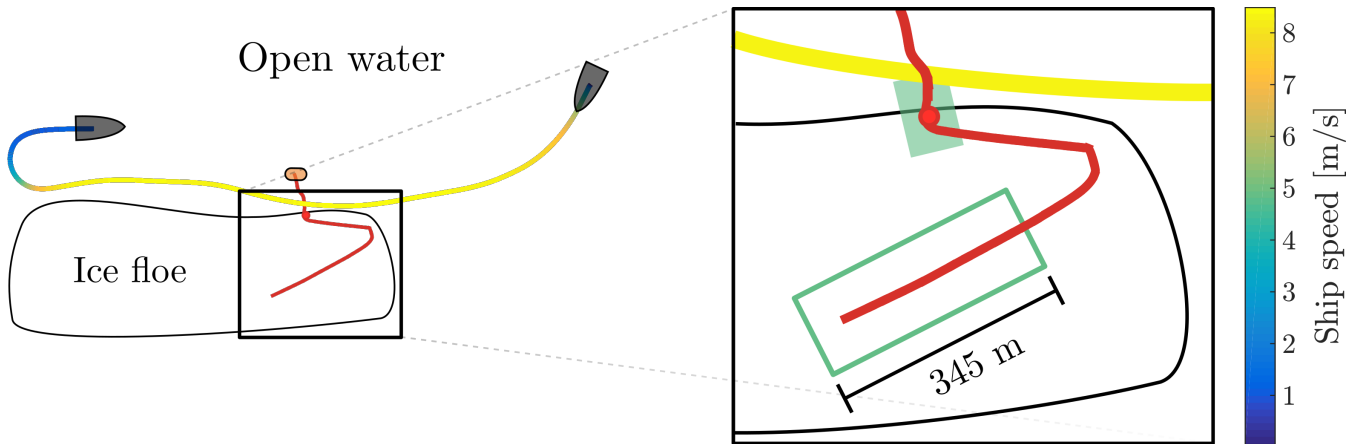


Figure 2. Schematic representation of the NBB experiment. The grey shape represents the ship and the orange ellipse the zodiac. The red and blue-to-yellow lines are respectively the UAV and ship GPS tracks. The solid green rectangle is the area of the panoramic picture selected for analysis (Figure 8). The approximate shape of the ice floe is also shown. To the bottom is an overview image of the *CCGS Amundsen* and the selected floe after break-up.

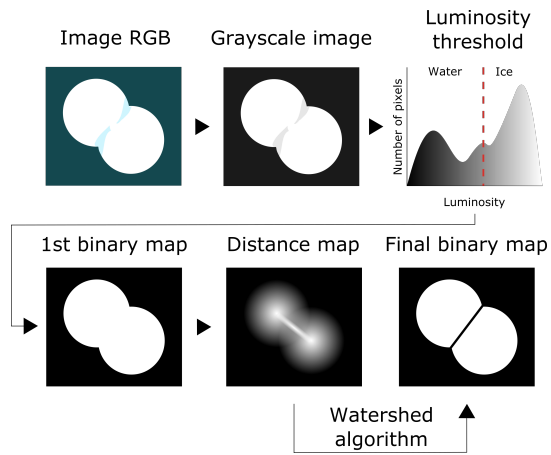


Figure 3. Steps of the image processing algorithm used for the boundary identification of floes in the GSL experiment.



Figure 4. Sample of the ellipses fitted on the ice floes by Matlab. Yellow and blue lines indicate the major and minor axes of length a and d , respectively.

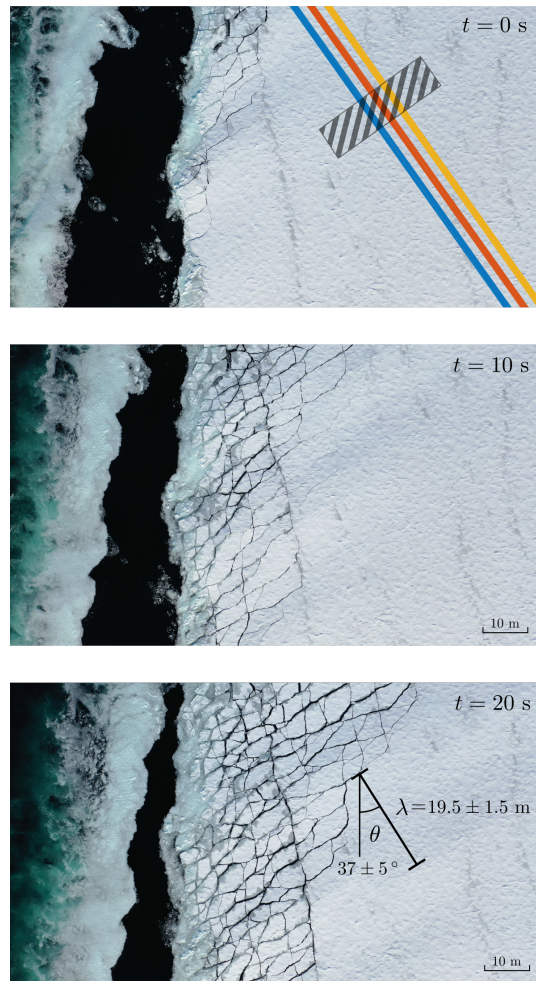


Figure 5. Snapshots of the wave-induced break-up experiment at $t = 0$, $t = 10$ s and $t = 20$ s. Waves are visible in the ice prior to break-up with $\lambda = 19.5 \pm 1.5$ m. Colored polygons in the top panel were used to calculate the break-up speed, and the dashed rectangle is the region of interest (ROI) used for the estimation of wave period.

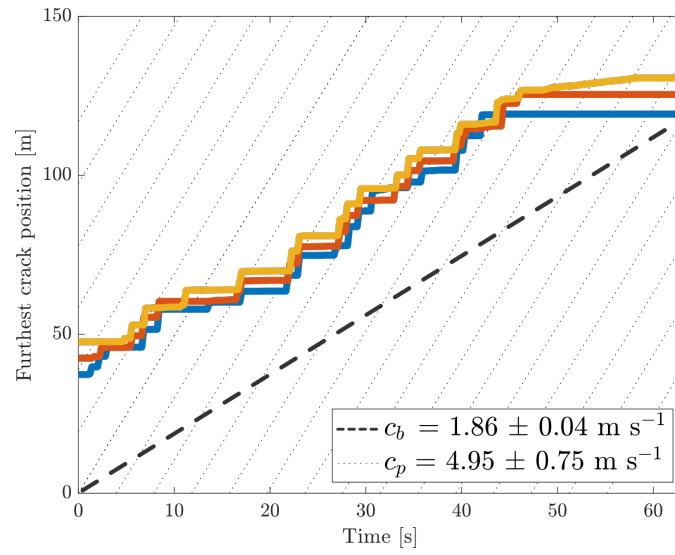


Figure 6. Temporal evolution of the furthest crack location relative to the floe edge at $x = 0$ along the three colored polygons shown in Fig. 5. Dotted lines indicate position of wave crests while the slope of the bold dashed line is obtained from the linear regression.

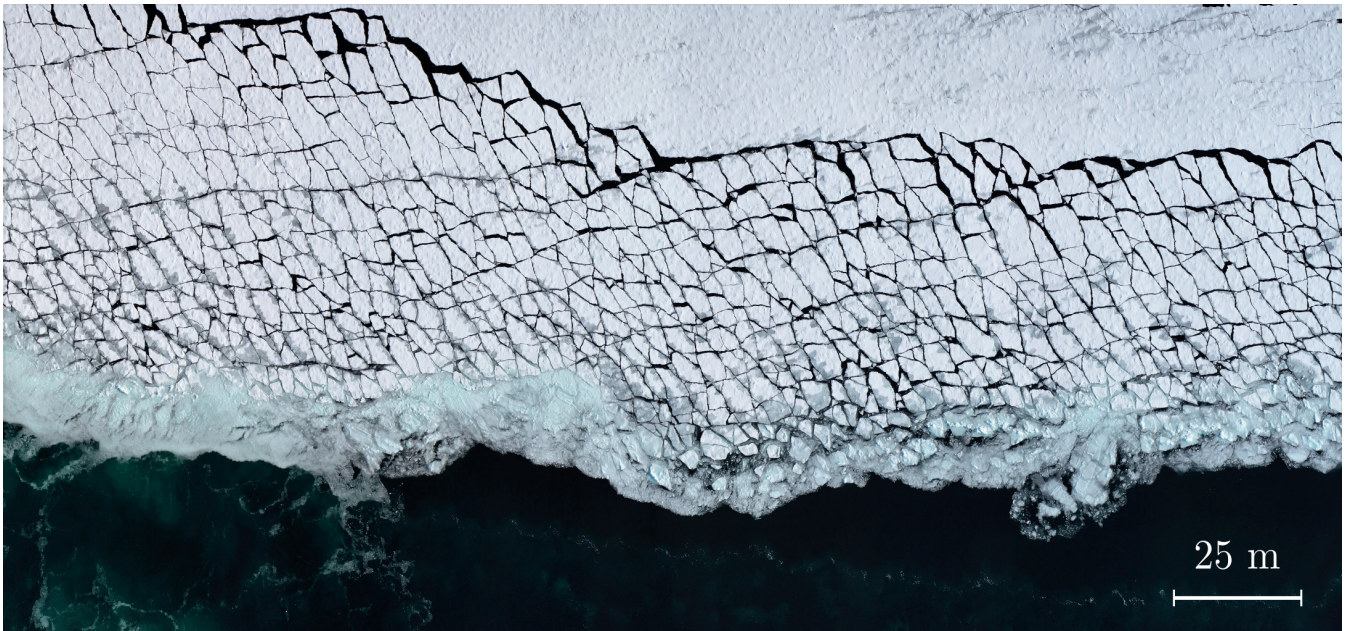


Figure 7. Break-up resulting from the GSL experiment. The ship sailed along the horizontal axis of the image.

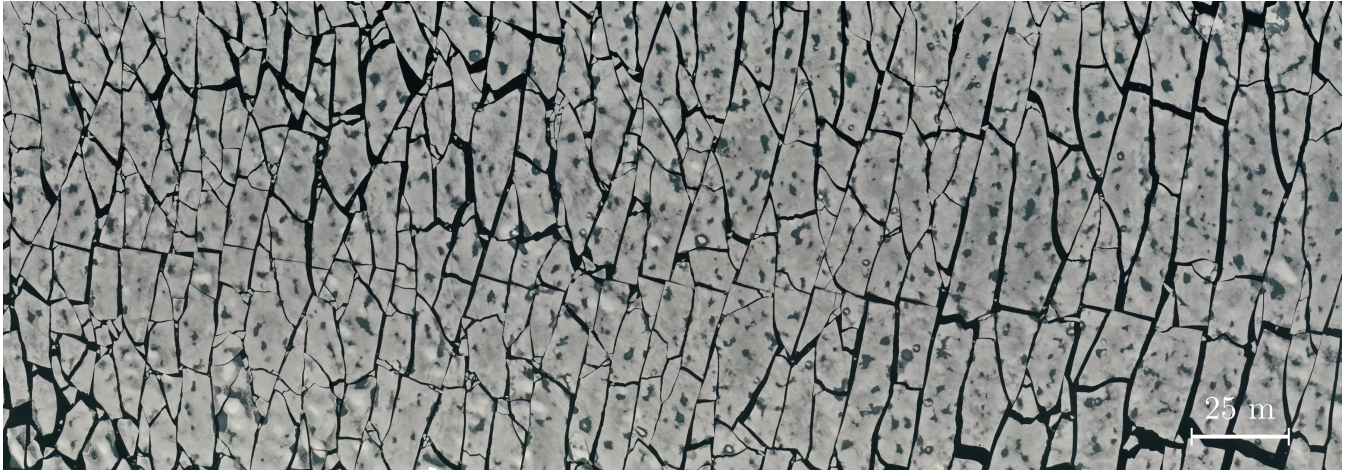


Figure 8. Partial view of the break-up resulting from the NBB experiment, corresponding to the green rectangle in Figure 2.

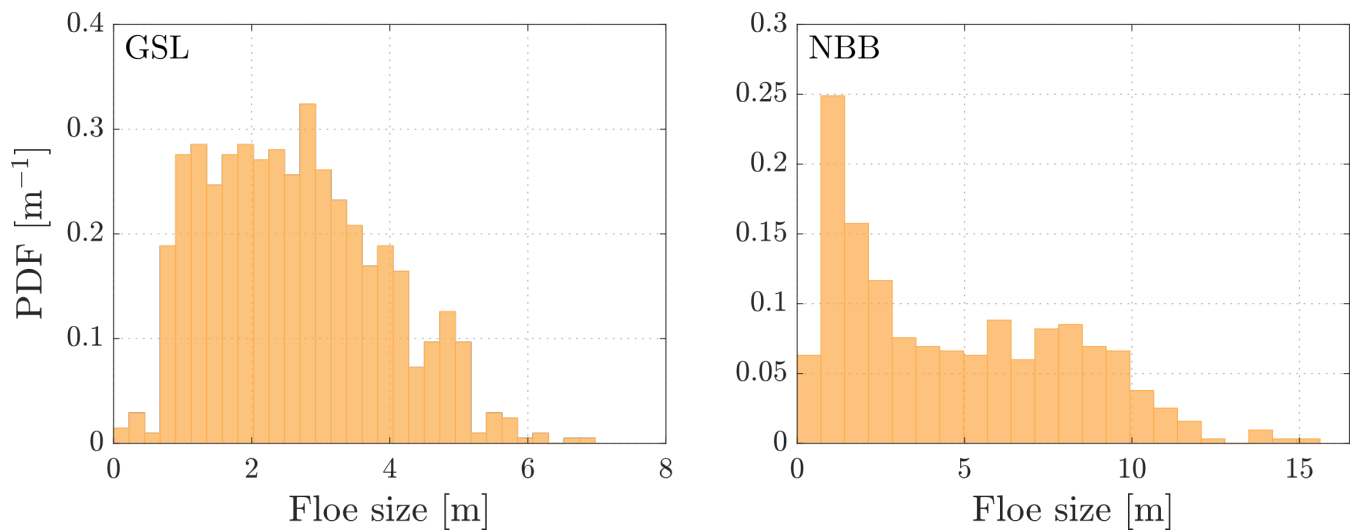


Figure 9. Number-based probability density functions of floe size (NFSDs) resulting from the break-up experiments.

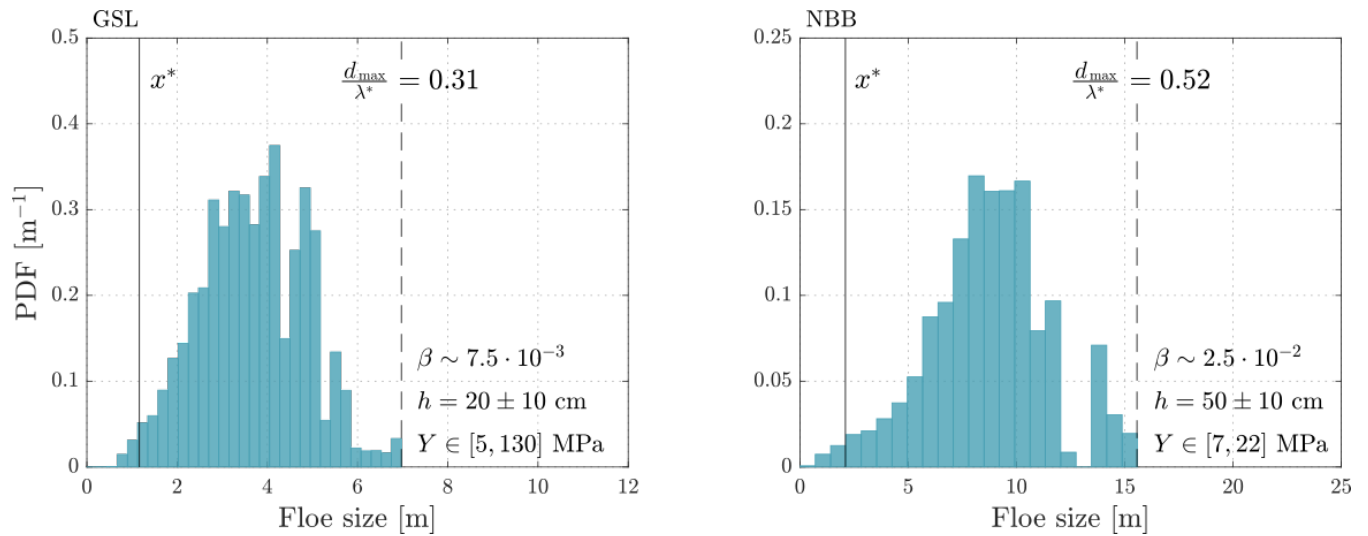


Figure 10. Area-based floe size distributions (AFSD) resulting from the break-up experiments computed with Eq. (3). The maximal floe size is compared to λ^* , the wavelength of the highest amplitude ship-generated wave estimated using Eq. (1), and to x^* , the flexural rigidity length scale given by Eq. (10) with values of Y derived from Tkacheva (2001).

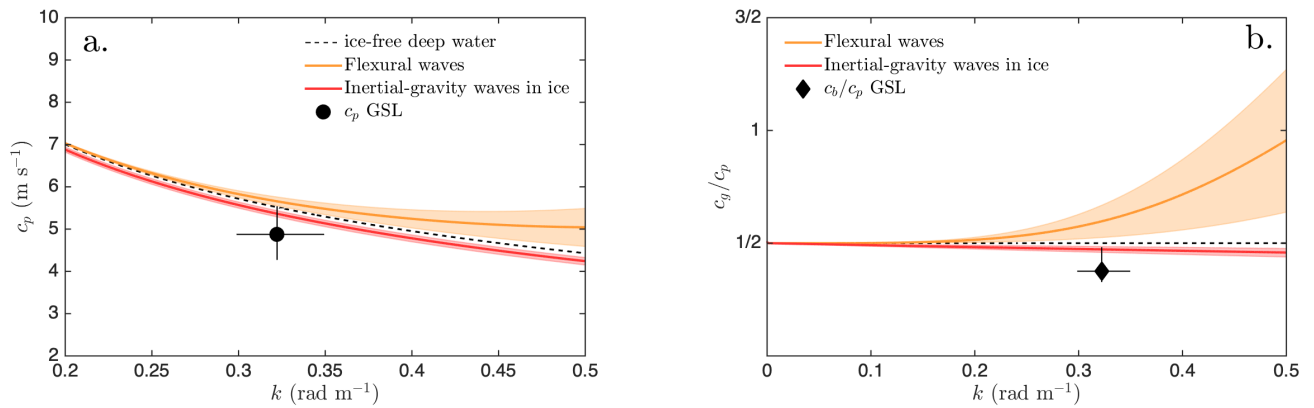


Figure 11. Phase speed (a) and ratio between the group speed and the phase speed (b) as a function of wavenumber k for ice-free deep water waves (dash line), pure flexural waves (orange, Eq. 16 with $\rho_i = 0$) or pure inertial gravity waves (red, Eq. 16 with $Y = 0$). Mean and extreme values for ice thickness h and Young's modulus Y are those of Figure 10 and Table 2. The black diamond indicates the ratio between the break-up speed c_b and the measured phase speed c_p in the GSL experiment, with uncertainties described in Table 1.